EUROPEAN JOURNAL OF COMPUTATIONAL MECHANICS, 2015
VOL. 24, NO. 4, 144–170, http://dx.doi.org/10.1080/17797179.2015.1096674

Taylor & Francis
Taylor & Francis Group

A 3D multiscale cohesive zone model for quasi-brittle materials accounting for friction, damage and interlocking

M. Albarella[a], R. Serpieri[a], G. Alfano[b] and E. Sacco[c]

[a]Dipartimento di Ingegneria, Università degli Studi del Sannio, Piazza Roma, 21 - I. 82100, Benevento, Italy; [b]Department of Mechanical, Aerospace and Civil Engineering, Brunel University, Uxbridge, UB8 3PH, UK; [c]Dipartimento di Ingegneria Civile e Meccanica, Università di Cassino e del Lazio Meridionale, Cassino, FR, Italy

ABSTRACT

A three-dimensional (3D) two-scale Cohesive Zone Model (CZM), which is based on a multiplane approach and couples damage with friction and interlocking, is presented for analysing crack propagation in quasi-brittle materials along structural interfaces where formation of cracks is expected. The main idea of the 3D multiplane formulation herein exploited is to describe the asperities of the interface in the form of periodic patterns of inclined planes, denominated Representative Interface Elements (RIE). The interaction within each plane of the RIE is governed by the interface formulation proposed by Alfano and Sacco in earlier work. After reporting details of the formulation and of its algorithmic implementation, the sensitivity of the macroscopic mechanical response to the specific selection of the RIE is analysed and reported with a general numerical assessment of the 3D interface mechanical response to monotonic and cyclic loading histories. A fundamental issue addressed in this paper is the identification of optimal RIE patterns with a minimum number of planes capable of providing isotropic in-plane behaviour in response to confined slip tests.

ARTICLE HISTORY
Received 1 April 2015
Accepted 17 September 2015

KEYWORDS
three-dimensional cohesive-zone model; interlocking; mixed-mode fracture; damage-friction coupling

1. Introduction

A proper account of friction and interlocking is frequently mandatory in the analysis of the mechanical response of quasi-brittle interfaces subjected to mixed-mode loading in presence of roughness of detached surfaces with a small-scale irregular geometry. Typical examples in which it is necessary to account for the presence of a small-scale irregular surface in the near-tip contact zone are mixed-mode decohesion of rock joint surfaces (Lee, Park, Cho, & You, 2001) and masonry-mortar joints (Rafsanjani, Loureno, & Peixinho, 2014). In particular,

CONTACT R. Serpieri rserpier@unisannio.it

the occurrence of cracks with pronounced rough profiles across mortar joints, departing from the straight brick-mortar interfaces, is experimentally shown in Fouchal, Lebon, and Titeux (2009). The importance of accounting for nonplanar detached interfaces has been recognised also in the delamination of fiber-reinforced polymer laminates (Sørensen and Jacobsen, 2009).

The mathematical position of problems of thin adhesive layers characterised by roughness (modelled in the form of adhesive boundaries having highly oscillating properties), is addressed by Licht and Michaille (1997) and by Licht, Michaille, and Pagano (2007) in the framework of Γ-convergence, and with a specific focus on hyperelastic materials having nonconvex energy density.

Retaining a more specific engineering perspective and a focus on inelasticity, modelling of the above-mentioned decohesion phenomena can be approached by employing suitable thermodynamic potentials (Del Piero & Raous, 2010; Raous, Cangémi, & Cocu, 1999) or, alternatively, employing homogenisation procedures (Luciano & Sacco, 1997) combined with damage mechanics (Mauge & Kachanov, 1994), as shown, by particular, in Fouchal, Lebon, Raffa, and Vairo (2014) by performing a sensitivity analysis of the interface stiffness to an internal variable describing waviness of the rough cracked interface.

Within this last family of approaches for the mechanical modelling of adhesive interfaces, Cohesive Zone Models (CZMs) (Mi, Crisfield, Davies, & Hellweg, 1998) are a widely employed technique for analysing crack propagation in structural interfaces within quasi-brittle materials along interfaces where formation and propagation of cracks are expected. Several interface models accounting for damage-friction coupling have been proposed in the literature, see, e.g. Del Piero and Raous (2010) and references therein. Some of them are based on nonassociative softening plasticity, such as the multidissipative interface model proposed by Cocchetti, Maier, and Shen (2001) and the contributions given by Bolzon and Cocchetti (2003) and by Červenka, Kishen, and Saouma (1998) in the field of concrete dams analysis, and by Giambanco, Rizzo, and Spallino (2001). A cohesive approach with separate values of the energy dissipation in mode I and mode II combined with a contact algorithm has been also recently investigated by Snozzi and Molinari (2013).

In Serpieri and Alfano (2011), a two-dimensional CZM, based on a simplified multiplane micromechanical formulation, has been recently proposed for coupling damage and friction in quasi brittle interfaces with irregular geometry at the small scale. The main idea of the multiplane formulation exploited in this reference is to describe the asperities of the interface in the form of a periodic arrangement of distinct inclined planes, denominated Representative Interface Element (RIE). The interaction within each of these surfaces is governed by the interface assumptions proposed by Alfano and Sacco (2006): 1) each infinitesimal area of microsurface is assumed to be decomposed into an undamaged and a fully damaged part; 2) the evolution of damage is assumed to depend on the elastic energy in the undamaged part; 3) it is assumed that friction occurs only on the damaged part and is

governed by a Coulomb law. Restraints to the model parameters stemming from thermodynamical consistency considerations have been derived and discussed by Serpieri, Sacco, and Alfano (2015).

This deterministic RIE approach suitably applies to surfaces with artificially constructed periodic roughness patterns such as deformed bars for reinforced concrete with regular rib patterns (Serpieri, Varricchio, Sacco, & Alfano, 2014). For natural rock joints, while a proper description of the asperity distribution demands a statistical treatment (Barton & Choubey, 1977; Brown and Scholz, 1985), a RIE deterministic description of asperities can be retained (Lee et al., 2001) with the main advantage of keeping the number of employed history variables limited.

Furthermore, in Serpieri, Sacco et al. (2015) it was shown that this approach allows developing a CZM where a unique value of purely 'rupture' energy is defined, which is the same in both opening and sliding modes. The reason is that the increase in total (measured) fracture energy normally found with increasing mode II/mode I ratio is retrieved because the total fracture energy in the model is the sum of the rupture energy and the energy dissipated by friction. The case of pure mode II also clearly indicates that not only friction but also the geometry of the fracture-surface asperities play an essential role in this modelling approach. Since the formulation by Serpieri, Sacco et al. (2015) allows decomposing the total dissipation into the different contributions given by rupture, friction and fracture asperities, it ultimately leads to a model which has a very sound physical foundation. As a result, its input parameters have a very clear mechanical meaning and, in the authors' opinion, are also easier to characterise through procedures that can be implemented in robust industrial standards.

The successful validation of the 2D model in Serpieri, Sacco et al. (2015) against experimental results reported for mixed-mode testing of a double cantilever beam in Sørensen and Jacobsen (2009) suggests that the extension of the approach to a general 3D model can lead to a very effective computational tool for the virtual simulation of the 3D complex features of failure in laminated composites in the context of real industrial applications (see for example Allegri, Jones, Wisnom, & Hallett, 2011; Charalambous, Allegri, Lander, & Hallett, 2015).

Capturing the 3D aspects of fracture propagation can be very important also in the other areas of engineering which were mentioned above, see just as one example the failure of masonry panels involving the combination of in-plane and out-of-plane behaviour considered by Macorini and Izzuddin (2011).

On the other hand, in all problems addressed by Serpieri and Alfano (2011), Serpieri et al. (2014) axial-symmetry or plane-stress and plane-strain conditions are invoked so as to admit a 2D formulation, and consider, accordingly, 2D RIEs.

Few works to date address full three-dimensional (3D) cohesive interface models in presence of both friction and interlocking. Most of them (see e.g. Foulk, Allen, & Helms, 2000; Evangelista, Roesler, & Proença, 2013; Gasser & Holzapfel, 2006; Cuvilliez, Feyel, Lorentz, & Michel-Ponnelle, 2012; Ruiz, Pandolfi, & Ortiz, 2001; Radovitzky, Seagraves, Tupek, & Noels, 2011) are focused on the prediction

of crack growth in materials without a specific account of roughness. A nonlinear interface element based upon a co-rotational approach and specifically devised to address three-dimensional decohesion problems has been recently presented by Macorini and Izzuddin (2011) to treat geometric nonlinearities arising in the collapse of masonry panels. The effect of large deformations in a 3D cohesive zone element has been also investigated in Van den Bosch, Schreurs, and Geers (2008). In Ho, Joshi, and Tay (2012), a 3D cohesive model is used to simulate the delamination of silicon devices due to thermal-induced stresses. In all of the above-mentioned works, a simplified approach is used to describe the mechanical behaviour of the interacting surfaces: friction and the effect of asperities are neglected, the simulations being limited to a pure mode-I fracture growth.

In the present contribution, an extension of the formulation proposed by Serpieri & Alfano (2011) to 3D problems is illustrated whereby the RIE is represented as a finite 3D pattern of inclined surfaces and the formulation allows defining relative displacements of the microsurfaces along three possible independent directions.

The generalisation of the RIE approach to three-dimensional kinematics is not trivial. Since the number of equations to be solved and history parameters to be updated at each structural iteration in each integration point is an increasing function of the number of planes in the RIE, a minimum number of planes is desirable, and the specific selection of the RIE is the result of a trade-off between computational cost and the sought level of accuracy in the interface response required to retrieve a realistic structural behaviour.

Is some cases, frictional anisotropy is a mechanical feature which cannot be excluded, in particular for surfaces especially engineered to obtain an anisotropic corrugation (Konyukhov, Vielsack, & Schweizerhof, 2008) and can be also originated as the effect of microstructure evolution induced by the kinematics of sliding itself (Zmitrowicz, 2006). When these particular cases are excluded, for statistically homogeneous surfaces with randomly distributed asperities, such as those in ordinary concrete and masonry, statistical in-plane isotropy of fractured surfaces represents a customary property of the interface response. In this respect, a fundamental issue to be addressed is thus the identification of optimal RIE patterns with a minimum number of planes, but capable of reproducing isotropic in-plane behaviour. In other words, the aim is to avoid spurious anisotropy effects possibly introduced by an excessive simplification with an insufficient number of inclined planes.

To address this issue, a sensitivity analysis has been also conducted and reported to illustrate the effects of the specific selection of the RIE geometry on the macroscopic mechanical response, in cases of monotonic and cyclic loading histories.

The paper is organised as follows: Section 2 describes the analytical formulation of the 3D multiplane model with coupled damage and friction while Section 3 discusses its numerical implementation. Numerical simulations are reported in

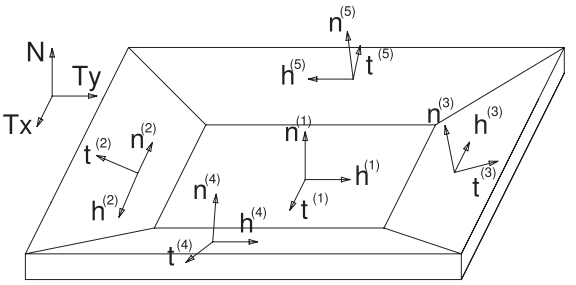

Figure 1. Example of RIE composed of 5 microplanes.

Section 4 and, finally, a discussion of the results is reported together with some conclusive remarks.

2. Formulation

2.1. Geometry and multiplane coupling

The Representative Interface Element (RIE), an example of which is shown in Figure 1, is composed of a pattern of N_p small-scale inclined planes. A global orthonormal reference frame is introduced with coordinates N, T_x, T_y and reference unit vectors $\mathbf{N}$, $\mathbf{T}_x$ and $\mathbf{T}_y$, with $\mathbf{N}$ being normal to the average interface plane and $\mathbf{T}_x$, $\mathbf{T}_y$ being orthogonal and contained in such plane. Subscripts N, X and Y are used to denote components of stresses and displacements relative to $\mathbf{N}$, $\mathbf{T}_x$ and $\mathbf{T}_y$.

Geometrical and mechanical quantities associated or contributed by the k-th microplane are denoted by a round bracketed superscript $(.)^{(k)}$. A local orthogonal reference frame is considered for each RIE-plane with coordinates $n^{(k)}$, $h^{(k)}$, $t^{(k)}$ whose respective unit vectors are oriented so that $\mathbf{n}^{(k)}$ is normal to plane k, while the other two tangential axes, for all surfaces with nonzero inclination to the average surface, are defined as:

$$\mathbf{h}^{(k)} = \frac{\mathbf{N} \times \mathbf{n}^{(k)}}{\|\mathbf{N} \times \mathbf{n}^{(k)}\|} \qquad \mathbf{t}^{(k)} = \mathbf{n}^{(k)} \times \mathbf{h}^{(k)} \tag{1}$$

According to (1), $\mathbf{h}^{(k)}$ axis is taken parallel to the average surface and $\mathbf{t}^{(k)}$ is directed along the line of maximum inclination over the average surface. In the trivial case of a plane k oriented as the average surface (i.e. $\mathbf{N}= \mathbf{n}^{(k)}$) local axes are taken coincident with global ones, i.e. $\mathbf{t}^{(k)}=\mathbf{T}_x$ and $\mathbf{h}^{(k)}=\mathbf{T}_y$.

Figure 1 shows an example of a RIE with five microplanes, with global and local reference frames.

The following kinematic and constitutive assumptions considered in Serpieri, Sacco et al. (2015) are here extended to the 3D case: 1) the RIE undergoes (locally) a rigid relative translation between the bottom and top surfaces, so that the relative displacement of each k-th microplane, $\mathbf{s}^{(k)}$, coincides with the relative displacement $\mathbf{s}$

of the whole surface; 2) the overall Helmoltz free energy density (per unit projected area onto the average plane), ψ, is contributed by planes as a linear combination of their respective energy densities $\psi^{(k)}$ in which the participation factor of the k -th plane is denoted by the symbol $\gamma^{(k)}$:

$$\mathbf{s} = \mathbf{s}^{(k)} \qquad \psi = \sum_{k=1}^{N_p} \gamma^{(k)} \psi^{(k)} \tag{2}$$

By differentiating $(2)_2$ with respect to the relative displacement, it is inferred that the global interface traction $\boldsymbol{\sigma}$ and the local interface traction $\boldsymbol{\sigma}^{(k)}$ contributed by the k-th microplane are related by an analogous linear combination with the same participation coefficients $\gamma^{(k)}$, viz.

$$\boldsymbol{\sigma} = \sum_{k=1}^{N_p} \gamma^{(k)} \boldsymbol{\sigma}^{(k)} \tag{3}$$

The next subsections detail the damage evolution law, the elastic response and the frictional response of the single inclined planes, which are described relative to the local microplane reference frames. The relevant local coordinates on plane k of $\mathbf{s}$ and $\boldsymbol{\sigma}^{(k)}$ are denoted by the sets of three symbols $s_n^{(k)}$, $s_t^{(k)}$, $s_h^{(k)}$ and $\boldsymbol{\sigma}_n^{(k)}$,$\boldsymbol{\tau}_t^{(k)}$,$\boldsymbol{\tau}_h^{(k)}$, respectively. Symbol $\boldsymbol{\tau}^{(k)}$ is used to denote the tangential component of the stress contributed by plane k, i.e. $\boldsymbol{\tau}^{(k)} = \boldsymbol{\sigma}^{(k)} - \boldsymbol{\sigma}_n^{(k)} \mathbf{n}^{(k)}$

2.2. Single plane model

The constitutive law of the k-th microplane, relating the stress $\boldsymbol{\sigma}^{(k)}$ to the displacement $\mathbf{s}^{(k)}$, is nonlinear and depends on the history of the past displacements.

The response of a given inclined plane (k) is such that, in absence of damage evolution and friction, the stress-relative displacement law is linear. Following Alfano and Sacco (2006), the surface of each microplane is decomposed into an undamaged part and a damaged part which contribute to the stress $\boldsymbol{\sigma}^{(k)}$ according to the following additive law

$$\boldsymbol{\sigma}^{(k)} = (1 - \alpha^{(k)}) \boldsymbol{\sigma}_u^{(k)} + \alpha^{(k)} \boldsymbol{\sigma}_d^{(k)} \tag{4}$$

where $\boldsymbol{\sigma}_d^{(k)}$, $\boldsymbol{\sigma}_u^{(k)}$ are the stresses contributed by the damaged and undamaged parts, respectively. The damage variable $\alpha^{(k)}$ is the ratio of the area of the damaged surface of plane k to the overall area of microplane k, with $0 \leq \alpha^{(k)} \leq 1$ being $\alpha^{(k)} = 0$ and $\alpha^{(k)} = 1$ associated with the undamaged and a fully damaged interface, respectively. The components of $\boldsymbol{\sigma}_d^{(k)}$ and $\boldsymbol{\sigma}_u^{(k)}$ in the local microplane reference are denoted by $\boldsymbol{\sigma}_{dn}^{(k)}$,$\boldsymbol{\tau}_{dt}^{(k)}$,$\boldsymbol{\tau}_{dh}^{(k)}$ for $\boldsymbol{\sigma}_d^{(k)}$ and $\boldsymbol{\sigma}_{un}^{(k)}$,$\boldsymbol{\tau}_{ut}^{(k)}$,$\boldsymbol{\tau}_{uh}^{(k)}$ for $\boldsymbol{\sigma}_u^{(k)}$. The tangential components of $\boldsymbol{\sigma}_d^{(k)}$ and $\boldsymbol{\sigma}_u^{(k)}$ are the vectors $\boldsymbol{\tau}_d^{(k)} = \tau_{dt}^{(k)} \mathbf{t}^{(k)} + \tau_{dh}^{(k)} \mathbf{h}^{(k)}$ and $\boldsymbol{\tau}_u^{(k)} = \tau_{ut}^{(k)} \mathbf{t}^{(k)} + \tau_{uh}^{(k)} \mathbf{h}^{(k)}$.

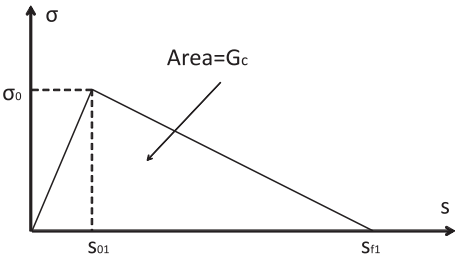

Figure 2. Mode I bilinear stress-displacement law of damage response.

2.2.1. Damage evolution law

The damage evolution law employed for each plane is a direct extension of the formulation proposed by Alfano and Sacco (2006), with the additional restrictions to the interface material parameters implied by the hypotheses considered in Serpieri, Sacco et al. (2015) and on account of the thermodynamic consistency requirements derived in the same reference. In particular, in the 3D extension herein considered of the opening-sliding formulation of Alfano and Sacco no distinction is made between sliding modes in relation to the direction of propagation of the crack front, so that global mode II and mode III, or a combination of the two, are all treated in the same way. Accordingly, the following material parameters are introduced:

- s_{01}, s_{02}: normal and tangential displacements at the onset of the damage in modes I and II, respectively;
- s_{f1} and s_{f2}: normal and tangential displacements at the point of complete rupture of the interface in modes I and II;
- G_{c1} and G_{c2}: fracture energies (of the single plane) in modes I and II;
- σ_{01}, σ_{02}: normal and tangential stresses of each individual inclined plane at the onset of the damage in modes I and II, respectively;
- η, termed ductility, defined as

$$\eta = 1 - \frac{s_{01}}{s_{f1}} \tag{5}$$

The following damage displacement norm is introduced, which is a natural extension of the 2D norm presented in Alfano and Sacco (2006):

$$\beta^{(k)} = \sqrt{\frac{\langle s_n^{(k)} \rangle_+^2}{s_{01}^2} + \frac{(s_t^{(k)})^2 + (s_h^{(k)})^2}{s_{02}^2}} - 1 \tag{6}$$

where angle brackets $\langle \cdot \rangle_+$ are used to denote the positive part, i.e. $\langle f \rangle_+ = \frac{|f|+f}{2}$.

With this definition of β, the damage evolution law of plane k is:

$$\alpha^{(k)} = \max_{history} \left\{ 0, \min \left\{ 1, \frac{1}{\eta} \left(\frac{\beta^{(k)}}{1 + \beta^{(k)}} \right) \right\} \right\} \tag{7}$$

When friction is excluded, and in the case of constant mixed-mode ratio (including pure mode I or pure mode II), equations (4), (5), (6), (7) determine the response shown in Figure 2.

As shown by Serpieri, Sacco et al. (2015), requirements of thermodynamic consistency and use of an associated complementary evolution law for damage introduce the following restrictions to the allowable model parameters (see remark) for the single planes:

$$G_{c1} = G_{c2}. \tag{8}$$

Remark 1 The equality in Equation (8) only regards the adhesion energies in opening and sliding mode on the single microplane. It has been shown, by comparison with experimental data, that the increase in total fracture energy, with increasing mode I/mode II ratio, is correctly captured by the model (Serpieri, Sacco et al., 2015). Such increase is the result of the interplay between friction, adhesion energy and the geometry of the fracture surface at the microscale. On the other hand, we are neglecting other types of dissipation, for example due to plasticity, viscoplasticity or viscoelasticity. In most materials, the adhesion energy on the single microplane is not only the result of rupture of elastic bonds, but it may also include these other types of dissipation, which may depend on the mode mixity and justify $G_{c1} \neq G_{c2}$ also on the single microplane. In some cases, this difference may not be negligible but measuring it would be a challenging task. In any case, we believe that if this difference is to be accounted for, it would be more appropriate to do so by introducing additional internal variables and related dissipation mechanisms, see e.g. Musto and Alfano (2015) in the case of viscoelastic dissipation. □

Furthermore, it was also shown in Serpieri, Sacco et al. (2015) that when an associated law for damage evolution is employed, in conjunction with an equivalent displacement norm for damage, the following additional restrictions apply to the allowable model parameters:

$$s_{01} = s_{02}, \qquad s_{f1} = s_{f2}. \tag{9}$$

Remark 2 Constraint (9) significantly reduces the number of independent material parameters of the model to be calibrated, which is an advantage for its practical use. On the other hand, the cost of this constraint in terms of predicting capability of the model is negligible. This is because, for most applications, the influence of a possible difference in the initial stiffness values and of the critical displacements (or equivalently the peak strengths) in different modes is negligible.

For problems in which it is important to consider different and independent values of the stiffness and strength in (local) opening and sliding modes on the single microplane, this hypothesis can be relaxed although the neat thermodynamic formulation presented in Serpieri, Sacco et al. (2015) would have to be modified. □

In the rest of the paper, different symbols are maintained for G_{c1} and G_{c2}, s_{01} and s_{02}, s_{f1} and s_{f2}, essentially to enhance the clarity of some formulas. It is worth noting, however, that in all numerical simulations, equal values are taken for material parameters, as dictated by (8) and (9), using the following symbols to denote the common values employed for the input material parameters:

$$s_0 = s_{01} = s_{02} \qquad s_f = s_{f1} = s_{f2} \qquad \boldsymbol{\sigma}_0 = \boldsymbol{\sigma}_{01} = \boldsymbol{\sigma}_{02} \qquad G_c = G_{c1} = G_{c2} \tag{10}$$

2.2.2. Elastic response

The stress contributed by the undamaged part of the microplane follows a linear law which for plane k reads:

$$\boldsymbol{\sigma}_u^{(k)} = \mathbf{K}\mathbf{s}^{(k)} \tag{11}$$

where $[\mathbf{K}] = diag(K_n, K_t, K_t)$, being K_n and K_t the normal and tangential stiffness.

Due to constraints (8), (9), a common value is given to K_n and K_t which can be directly related to the fracture energy by:

$$K_n = K_t = \frac{2G_c}{(1-\eta)s_f^2} \tag{12}$$

2.2.3. Frictional response

The contribution to the stress provided by the damaged part of the surface combines a unilateral elastic law for the normal component:

$$\boldsymbol{\sigma}_{dn}^{(k)} = K_n \langle s_n^{(k)} \rangle_+ \tag{13}$$

with a tangential component that follows a nonassociative Coulomb frictional law with tangential sliding (Simo & Hughes, 2008). In particular, the law employed falls within the class of perfect plasticity models since there is no hardening. Accordingly, the displacement is decomposed into an elastic and an inelastic part:

$$\mathbf{s}_d^{(k)} = \mathbf{s}_{de}^{(k)} + \mathbf{s}_{di}^{(k)} \tag{14}$$

where, as specified below, the inelastic part is entirely tangential, and the frictional stress is expressed as

$$\boldsymbol{\sigma}_d^{(k)} = \mathbf{K}\mathbf{s}_{de}^{(k)} = \mathbf{K}\left(\mathbf{s}_d^{(k)} - \mathbf{s}_{di}^{(k)}\right). \tag{15}$$

Altogether, Equations (13) and (15) can be written in the compact form:

$$\boldsymbol{\sigma}_d^{(k)} = \mathbf{H}\left(\mathbf{s}_d^{(k)} - \mathbf{s}_{di}^{(k)}\right) \tag{16}$$

where $\mathbf{H}$ is defined as the operator that in the local microplane reference frame is represented by the matrix $diag((1-u(s_n))K_{n0}, K_{t0}, K_{t0})$ and $u(\cdot)$ is the unit step function (or Heaviside function)

$$u(t) = \begin{cases} 1 & t > 0 \\ 0 & t \leq 0 \end{cases} \tag{17}$$

The evolution of the plastic variables $\mathbf{s}_{di}^{(k)}$, is described in the framework of nonassociated elastoplasticity (Alfano & Sacco, 2006; Simo & Hughes, 2008) by introducing the following functions: a yield (or threshold) function of Coloumb type:

$$\phi(\boldsymbol{\sigma}^{(k)}) = \mu\langle\boldsymbol{\sigma}_{dn}^{(k)}\rangle_- + \sqrt{(\tau_{dt}^{(k)})^2 + (\tau_{dh}^{(k)})^2} = \mu\langle\boldsymbol{\sigma}_{dn}^{(k)}\rangle_- + \parallel \boldsymbol{\tau}_d^{(k)} \parallel, \tag{18}$$

a nonassociated plastic potential function, which determines sliding in the tangential direction of microplane k.

$$g(\boldsymbol{\sigma}_d^{(k)}) = \sqrt{(\tau_{dt}^{(k)})^2 + (\tau_{dh}^{(k)})^2} = \parallel \boldsymbol{\tau}_d^{(k)} \parallel . \tag{19}$$

Following a common choice in computational inelasticity (Simo & Hughes, 2008), the plastic flow rate equation is expressed with the aid of a nonnegative plastic multiplier $\lambda^{(k)}$

$$\dot{\mathbf{s}}_{di}^{(k)} = \dot{\lambda}^{(k)} \frac{\partial g}{\partial \boldsymbol{\sigma}_d^{(k)}} = \dot{\lambda}^{(k)} \begin{bmatrix} 0 \\ \frac{\partial g}{\partial \tau_{dt}^{(k)}} \\ \frac{\partial g}{\partial \tau_{dh}^{(k)}} \end{bmatrix} = \dot{\lambda}^{(k)} \begin{bmatrix} 0 \\ \frac{\tau_{dt}^{(k)}}{\sqrt{(\tau_{dt}^{(k)})^2 + (\tau_{dh}^{(k)})^2}} \\ \frac{\tau_{dt}^{(k)}}{\sqrt{(\tau_{dt}^{(k)})^2 + (\tau_{dh}^{(k)})^2}} \end{bmatrix} = \dot{\lambda}^{(k)} \begin{bmatrix} 0 \\ \frac{\tau_{dt}^{(k)}}{\|\boldsymbol{\tau}_d^{(k)}\|} \\ \frac{\tau_{dh}^{(k)}}{\|\boldsymbol{\tau}_d^{(k)}\|} \end{bmatrix} \tag{20}$$

and by introducing Kuhn–Tucker conditions (Kuhn & Tucker, 1951) to address the irreversible nature of frictional sliding:

$$\dot{\lambda}^{(k)} \geq 0 \qquad \phi(\boldsymbol{\sigma}_d^{(k)}) \leq 0 \qquad \dot{\lambda}^{(k)}\phi(\boldsymbol{\sigma}_d^{(k)}) = 0 \tag{21}$$

3. Numerical integration

Using a Newton-Raphson solution scheme, the time interval of the analysis is decomposed into a sequence of time increments. Let $(\cdot)^{\tau}$ and $(\cdot)^{\tau+\Delta\tau}$ denote the values of the variable $(\cdot)$ at the beginning and at the end of timestep. At the generic timestep $[\tau, \tau+\Delta\tau]$, the known variables are $\mathbf{s}^{(k),\tau}$, $\mathbf{s}^{(k),\tau+\Delta\tau}$, and the history variables $s_{dit}^{(k),\tau}$, $s_{dih}^{(k),\tau}$, $\alpha^{(k),\tau}$. The unknowns are the stress $\boldsymbol{\sigma}^{(k),\tau+\Delta\tau}$ and the updated history variables $s_{dit}^{(k),\tau+\Delta\tau}$, $s_{dih}^{(k),\tau+\Delta\tau}$, $\alpha^{(k),\tau+\Delta\tau}$.

The computation of the stress and of the updated inelastic history variables is obtained by solving for each of the microplanes the discretised form of the equations introduced in Section 2 in the interval $[\tau, \tau + \Delta\tau]$. Following a consolidated technique for perfect plasticity models (Simo & Hughes, 2008), the solution technique employed herein consists of an elastic predictor-inelastic correction algorithm, with a Backward Euler scheme of integration, linear interpolation over time and the inelastic correction implemented via a return mapping technique.

Discretisation of Equations (4), (6), (7), (16), (20) and (21) results in the following finite-step relations:

$$\boldsymbol{\sigma}^{(k),\tau+\Delta\tau} = (1-\alpha^{(k),\tau+\Delta\tau})\mathbf{K}\mathbf{s}^{(k),\tau+\Delta\tau} + \alpha^{(k),\tau+\Delta\tau}\boldsymbol{\sigma}_d{}^{(k),\tau+\Delta\tau} \tag{22}$$

$$\left[\boldsymbol{\sigma}_d{}^{(k),\tau+\Delta\tau}\right] = \left[\mathbf{H}^{(k),\tau+\Delta\tau}\right]\left(\left[\mathbf{s}^{(k),\tau+\Delta\tau}\right] - \left[\mathbf{s}_{di}^{(k),\tau+\Delta\tau}\right]\right) \tag{23}$$

$$\beta^{(k),\tau+\Delta\tau} = \sqrt{\frac{\langle s_n^{(k),\tau+\Delta\tau}\rangle_+^2}{s_{01}^2} + \frac{(s_t^{(k),\tau+\Delta\tau})^2 + (s_h^{(k),\tau+\Delta\tau})^2}{s_{02}^2}} - 1 \tag{24}$$

$$\alpha^{(k),\tau+\Delta\tau} = \max\left\{\alpha^{(k),\tau}, \min\left\{1, \frac{1}{\eta}\cdot\frac{\beta^{(k),\tau+\Delta\tau}}{1+\beta^{(k),\tau+\Delta\tau}}\right\}\right\} \tag{25}$$

$$\mathbf{s}_{di}{}^{(k),\tau+\Delta\tau} = \mathbf{s}_{di}{}^{(k),\tau} + \Delta\lambda^{(k)}\begin{bmatrix} 0 \\ \frac{\tau_{dt}^{(k),\tau+\Delta\tau}}{\|\boldsymbol{\tau}_d^{(k),\tau+\Delta\tau}\|} \\ \frac{\tau_{dh}^{(k),\tau+\Delta\tau}}{\|\boldsymbol{\tau}_d^{(k),\tau+\Delta\tau}\|} \end{bmatrix} \tag{26}$$

$$\Delta\lambda^{(k)} \geq 0 \tag{27}$$

$$\mu\langle\boldsymbol{\sigma}_{dn}^{(k),\tau+\Delta\tau}\rangle_- + \| \boldsymbol{\tau}_d^{(k),\tau+\Delta\tau} \| \leq 0 \tag{28}$$

$$\Delta\lambda^{(k)}(\mu\langle\boldsymbol{\sigma}_{dn}^{(k),\tau+\Delta\tau}\rangle_- + \| \boldsymbol{\tau}_d^{(k),\tau+\Delta\tau} \|) = 0 \tag{29}$$

Updating of $\beta^{(k)}$ and $\alpha^{(k)}$ is trivial since Equations (24) and (25) are explicit functions of the updated displacements and uncoupled from the remaining equations of the system. In contrast, solution of Equations (23), (26), (29) and inequalities (27) and (28) is nontrivial and is achieved by an elastic prediction and inelastic correction scheme which is described in detail below. Upon evaluating $\boldsymbol{\sigma}_d^{(k),\tau+\Delta\tau}$, as a final step, Equation (22) can be solved for the updated stress $\boldsymbol{\sigma}^{(k),\tau+\Delta\tau}$.

The elastic stress trial value with "frozen" inelastic displacement is computed first (elastic prediction):

$$\left[\boldsymbol{\sigma}_{de}{}^{(k),\tau+\Delta\tau}\right] = \left[\mathbf{H}^{(k),\tau+\Delta\tau}\right]\left(\left[\mathbf{s}^{(k),\tau+\Delta\tau}\right] - \left[\mathbf{s}_{di}^{(k),\tau}\right]\right) \tag{30}$$

together with the trial value of the yield function $\phi\left(\boldsymbol{\sigma}_{de}{}^{(k),\tau+\Delta\tau}\right)$.

If the trial value of the yield function is negative, then no evolution of inelastic variables takes place. Consequently, $\Delta\lambda^{(k)} = 0$ and the updated state is the following:

$$\begin{cases} \mathbf{s}_{di}^{(k),\tau+\Delta\tau} = \mathbf{s}_{di}^{(k),\tau} \\ \left[\boldsymbol{\sigma}_d{}^{(k),\tau+\Delta\tau}\right] = \left[\mathbf{H}^{(k),\tau+\Delta\tau}\right]\left(\left[\mathbf{s}^{(k),\tau+\Delta\tau}\right] - \left[\mathbf{s}_{di}^{(k),\tau+\Delta\tau}\right]\right) \\ \boldsymbol{\sigma}^{(k),\tau+\Delta\tau} = (1-\alpha^{(k),\tau+\Delta\tau})\mathbf{K}\mathbf{s}^{(k),\tau+\Delta\tau} + \alpha^{(k),\tau+\Delta\tau}\boldsymbol{\sigma}_d{}^{(k),\tau+\Delta\tau} \end{cases} \tag{31}$$

Conversely, if $\phi\left(\boldsymbol{\sigma}_{de}{}^{(k),\tau+\Delta\tau}\right)$ is positive, it must be $\Delta\lambda^{(k)} > 0$, otherwise the condition $\mathbf{s}_{di}^{(k),\tau+\Delta\tau} = \mathbf{s}_{di}^{(k),\tau}$ implied by Equation (26) would result in a positive yield function, in contrast with inequality (27). In this case, one infers from (29) that $\phi(\boldsymbol{\sigma}_d^{(k),\tau+\Delta\tau}) = 0$ and from (23) the following inelastic correction for the elastic stress is obtained:

$$\begin{aligned} \left[\boldsymbol{\sigma}_d{}^{(k),\tau+\Delta\tau}\right] &= \left[\mathbf{H}^{(k),\tau+\Delta\tau}\right]\left(\left[\mathbf{s}^{(k),\tau+\Delta\tau}\right] - \left[\mathbf{s}_{di}^{(k),\tau+\Delta\tau}\right]\right) \\ &= \left[\mathbf{H}^{(k),\tau+\Delta\tau}\right]\left(\left[\mathbf{s}^{(k),\tau+\Delta\tau}\right] - \left[\mathbf{s}_{di}^{(k),\tau}\right]\right) - \left[\mathbf{H}^{(k),\tau+\Delta\tau}\right]\left(\left[\mathbf{s}_{di}^{(k),\tau+\Delta\tau}\right] - \left[\mathbf{s}_{di}^{(k),\tau}\right]\right) \\ &= \left[\boldsymbol{\sigma}_{de}{}^{(k),\tau+\Delta\tau}\right] - \Delta\lambda^{(k)}\begin{bmatrix} 0 \\ K_{t0}\dfrac{\boldsymbol{\tau}_{dt}^{(k),\tau+\Delta\tau}}{\|\boldsymbol{\tau}_d^{(k),\tau+\Delta\tau}\|} \\ K_{t0}\dfrac{\boldsymbol{\tau}_{dh}^{(k),\tau+\Delta\tau}}{\|\boldsymbol{\tau}_d^{(k),\tau+\Delta\tau}\|} \end{bmatrix} \end{aligned} \tag{32}$$

The three scalar equations of (32), combined with the condition $\phi(\boldsymbol{\sigma}_d^{(k),\tau+\Delta\tau}) = 0$ form the following nonlinear system which is written again in the local frame of plane k:

$$\boldsymbol{\sigma}_{dn}{}^{(k),\tau+\Delta\tau} = \boldsymbol{\sigma}_{den}{}^{(k),\tau+\Delta\tau} \tag{33}$$

$$\tau_{dt}{}^{(k),\tau+\Delta\tau} = \tau_{det}{}^{(k),\tau+\Delta\tau} - \Delta\lambda^{(k)}K_{t0}\frac{\boldsymbol{\tau}_{dt}^{(k),\tau+\Delta\tau}}{\|\,\boldsymbol{\tau}_d^{(k),\tau+\Delta\tau}\,\|} \tag{34}$$

$$\tau_{dh}{}^{(k),\tau+\Delta\tau} = \tau_{deh}{}^{(k),\tau+\Delta\tau} - \Delta\lambda^{(k)}K_{t0}\frac{\boldsymbol{\tau}_{dh}^{(k),\tau+\Delta\tau}}{\|\,\boldsymbol{\tau}_d^{(k),\tau+\Delta\tau}\,\|} \tag{35}$$

$$\mu\langle\boldsymbol{\sigma}_{dn}^{(k),\tau+\Delta\tau}\rangle_- + \|\,\boldsymbol{\tau}_d^{(k),\tau+\Delta\tau}\,\| = 0 \tag{36}$$

where $\boldsymbol{\sigma}_{den}{}^{(k),\tau+\Delta\tau}$, $\tau_{det}{}^{(k),\tau+\Delta\tau}$, $\tau_{deh}{}^{(k),\tau+\Delta\tau}$ denote the components of $\boldsymbol{\sigma}_{de}{}^{(k),\tau+\Delta\tau}$.

The system above can be solved by deriving an equation in the only unknown $\Delta\lambda^{(k)}$. Accordingly, taking the norm of Equations (34) and (35), the following relation is inferred:

$$\|\,\boldsymbol{\tau}_d{}^{(k),\tau+\Delta\tau}\,\| = \frac{\|\,\boldsymbol{\tau}_{de}{}^{(k),\tau+\Delta\tau}\,\|}{1+\Delta\lambda^{(k)}\dfrac{K_{t0}}{\|\boldsymbol{\tau}_d^{(k),\tau+\Delta\tau}\|}} \tag{37}$$

and using Equations (33) and (36) to replace $\|\,\boldsymbol{\tau}_d{}^{(k),\tau+\Delta\tau}\,\|$ with $\boldsymbol{\sigma}_{den}{}^{(k),\tau+\Delta\tau}$, one finally obtains:

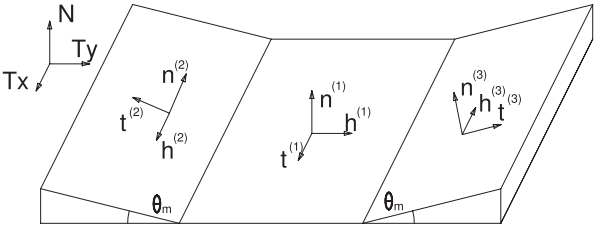

Figure 3. RIE made up of three microplanes employed in the simulations 4.1.

$$\Delta\lambda^{(k)} = \frac{1}{K_{t0}}\left(\mu\boldsymbol{\sigma}_{den}^{(k),\tau+\Delta\tau} + \| \boldsymbol{\tau}_{de}^{(k),\tau+\Delta\tau} \|\right) \tag{38}$$

Consequently, the solution of the system of Equations (33), (34), (35) and (36) is:

$$\begin{cases} \Delta\lambda^{(k)} = \frac{1}{K_{t0}}\left(\mu\boldsymbol{\sigma}_{den}^{(k),\tau+\Delta\tau} + \| \boldsymbol{\tau}_{de}^{(k),\tau+\Delta\tau} \|\right) \\ \boldsymbol{\sigma}_{dn}^{(k),\tau+\Delta\tau} = \boldsymbol{\sigma}_{den}^{(k),\tau+\Delta\tau} \\ \tau_{dt}^{(k),\tau+\Delta\tau} = -\mu\boldsymbol{\sigma}_{den}^{(k),\tau+\Delta\tau}\frac{\tau_{det}^{(k),\tau+\Delta\tau}}{\|\boldsymbol{\tau}_{de}^{(k),\tau+\Delta\tau}\|} \\ \tau_{dh}^{(k),\tau+\Delta\tau} = -\mu\boldsymbol{\sigma}_{den}^{(k),\tau+\Delta\tau}\frac{\tau_{deh}^{(k),\tau+\Delta\tau}}{\|\boldsymbol{\tau}_{de}^{(k),\tau+\Delta\tau}\|} \end{cases} \tag{39}$$

Once $\Delta\lambda^{(k)}$ is determined, the updated state of the interface is completely known as the updated inelastic displacement $\mathbf{s}_{di}^{(k),\tau+\Delta\tau}$ can be computed from Equation (26) and the updated stresses $\boldsymbol{\sigma}_d{}^{(k),\tau+\Delta\tau}$, $\boldsymbol{\sigma}^{(k),\tau+\Delta\tau}$ are given by Equations (22) and (23), respectively.

4. Numerical examples

The algorithmic procedure of Section 3 was applied to integrate the CZM described in Section 2 and several numerical analyses were carried out. The present section reports the results of four sets of numerical examples. Section 4.1 illustrates the results of a first group of numerical analyses whose objective is to assess that the 3D formulation presented in this paper reproduces the response obtained in the 2D formulation proposed by Serpieri, Sacco et al. (2015), Serpieri and Alfano (2011). The examples in Section 4.2 illustrate the general behaviour exhibited by the present 3D formulation by reporting the results of simulations performed employing the five-plane RIE shown in Figure 1. Section 4.3 shows the results of simulations performed under zero normal stress, whose aim is to elucidate the energy behaviour of the model in relation to sliding direction, mode mixity and

Table 1. Normals to the RIE-planes employed in the simulations of Section 4.1

	$k = 1$	$k = 2$	$k = 3$
$n_N^{(k)}$	1.0	$\cos\theta_m$	$\cos\theta_m$
$n_{T_x}^{(k)}$	0.0	$\sin\theta_m$	$-\sin\theta_m$
$n_{T_y}^{(k)}$	0.0	0.0	0.0
$\gamma^{(k)}$	0.3333	0.3333	0.3333

Table 2. Material parameters employed in the simulations of Section 4.1. Note that $G_{c1} = G_{c2} = G_c$ and $\boldsymbol{\sigma}_{01} = \boldsymbol{\sigma}_{02} = \boldsymbol{\sigma}_0$ as stated in Section 2.

$\boldsymbol{\sigma}_0$ [MPa]	G_c [KJ/m^2]	η [–]	μ [–]
3.0	0.3	0.9	0.5

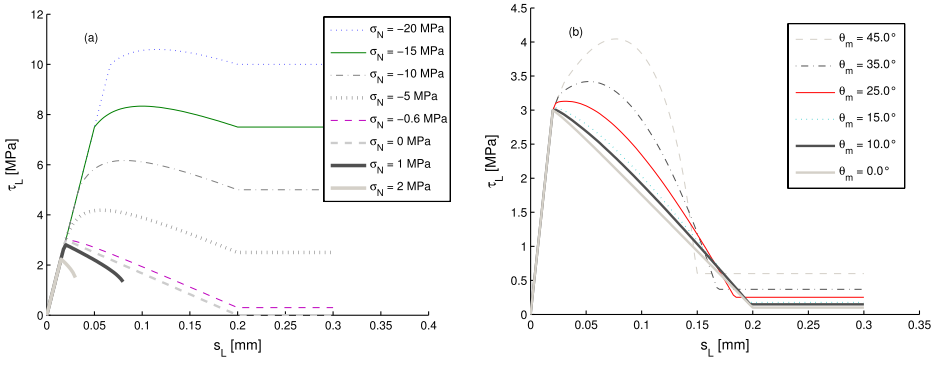

Figure 4. (a) $\tau_L - s_L$ curves with $\theta_m = 0°$ (perfectly flat RIE) for a monotonic slip history. This plot can be compared with Figure 3 in Serpieri and Alfano (2011); (b) $\tau_L - s_L$ curves with variable θ_m for a monotonic load history. This plot can be compared with Figure 4 in Serpieri and Alfano (2011).

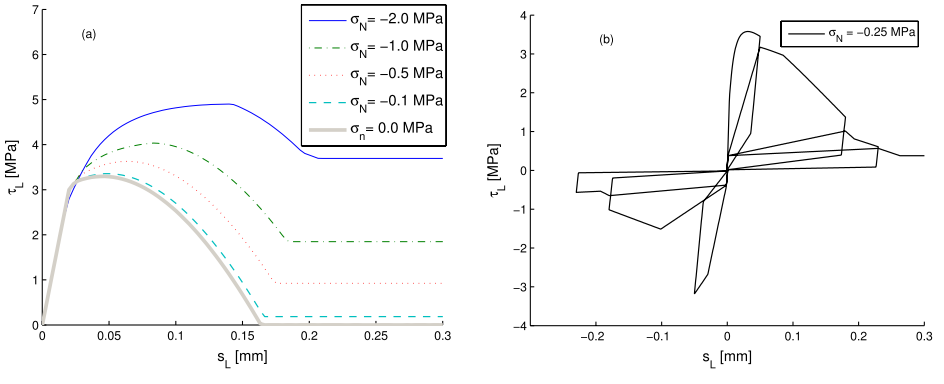

Figure 5. (a) tau-slip plots with $\theta_m = 35°$ for a monotonic load history. This plot can be compared with Figure 5 in Serpieri and Alfano (2011); (b) tau-slip curves with $\theta_m = 30°$ for a cyclic load history with slip sign reversal. This plot can be compared with Figure 13 in Serpieri and Alfano (2011).

decohesion path. The last set of simulations, described in Section 4.4, consists of parametric analyses aimed at the optimal selection of a RIE pattern capable of providing an isotropic response in the average plane.

4.1. Consistency between 2D and 3D responses

The three-dimensional pattern with plane symmetry and trapezoid section shown in Figure 3 was selected as RIE to run a first set of analyses of the tangential stress-slip model response under constant confining stress and prescribed tangential slip. This RIE reproduces under three-dimensional kinematics the 2D pattern employed by Serpieri, Sacco et al. (2015) and Serpieri and Alfano (2011). Accordingly, it is composed of three microplanes with equal area fractions $\gamma^{(k)} = 1/3$, whose normals are specified in Table 1, corresponding to one horizontal plane and two additional planes inclined by an angle $\mp\theta_m$ to the average plane. The interface is subjected to an applied constant normal stress $\boldsymbol{\sigma}_N$ while sliding s_L is enforced along the T_y axis with null relative displacement along the T_x direction.

The material parameters employed in the simulations of this section are those considered in Section 4.1 of the article by Serpieri and Alfano (2011) and are recalled in Table 2.

To assess the consistency of the 3D and 2D formulations, the interface response is investigated by reproducing the families of $\tau_L - s_L$ plots (with τ_L being the global tangential tress in the T_x direction) considered in three numerical examples by Serpieri and Alfano (2011).

Specifically:

- Figure 4(a) shows the family of $\tau_L - s_L$ curves obtained under a monotonic slip history along T_y axis with $\boldsymbol{\sigma}_N$ spanning the range $[-20\ MPa, 2\ MPa]$ and $\theta_m = 0°$ (perfectly flat RIE). This plot can be compared with Figure 3 of the article by Serpieri and Alfano (2011).
- Figure 4(b) shows the family of $\tau_L - s_L$ curves with $\boldsymbol{\sigma}_N = -10\ MPa$ and θ_m spanning the interval $[0°, 45°]$ and with a monotonic load history along T_y axis. This plot can be compared with Figure 4 of the article by Serpieri and Alfano (2011).
- Figure 5(a) shows the family of $\tau_L - s_L$ plots obtained by spanning $\boldsymbol{\sigma}_N$ in the range $[-2\ MPa, 0\ MPa]$ and with $\theta_m = 35°$ and a monotonic load history along T_y axis. This plot can be compared with Figure 5 of the article by Serpieri and Alfano (2011).
- Figure 5(b) contains the $\tau_L - s_L$ plot for a fixed value of $\boldsymbol{\sigma}_N = -10\ MPa$ and $\theta_m = 30°$ obtained under a cyclic load history with slip sign reversal along T_y axis. This plot can be compared with Figure 13 of the article by Serpieri and Alfano (2011).

The results of these simulations match those of the 2D simulations reported by Serpieri and Alfano (2011), which confirms the consistent recovery from the

Table 3. RIE pattern (normals and area fractions) employed in the simulations of Section 4.2.

	$k=1$	$k=2$	$k=3$	$k=4$	$k=5$
$n_N^{(k)}$	1.0	$\cos\theta_m$	$\cos\theta_m$	$\cos\theta_m$	$\cos\theta_m$
$n_{T_x}^{(k)}$	0.0	$\sin\theta_m$	$-\sin\theta_m$	0.0	0.0
$n_{T_y}^{(k)}$	0.0	0.0	0.0	$\sin\theta_m$	$-\sin\theta_m$
$\gamma^{(k)}$	0.2	0.2	0.2	0.2	0.2

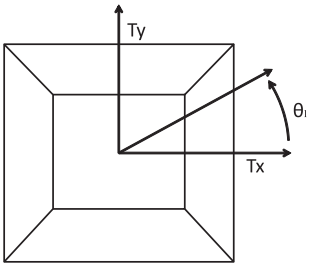

Figure 6. Plan view of the RIE used in the examples of Section 4.2 showing how θ_L defines the direction of the impressed sliding.

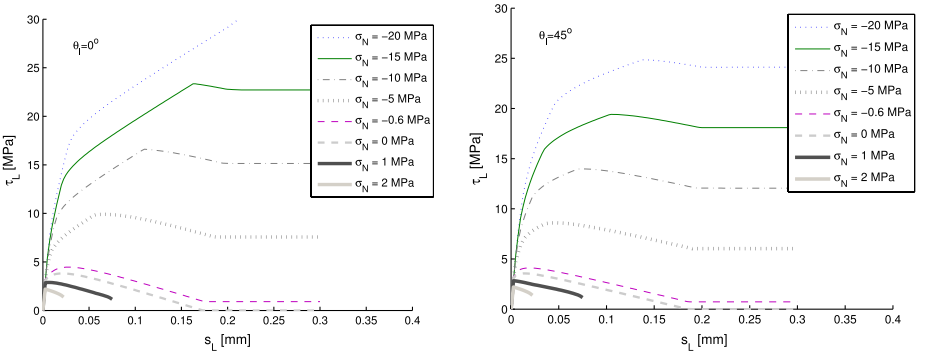

Figure 7. $\tau_L - s_L$ curves with $\theta_m = 30°$, monotonic load history along (a) $\theta_L = 0°$ and (b) $\theta_L = 45°$.

current 3D formulation of the 2D model proposed by Serpieri and Alfano (2011) and its correct implementation.

Remark 3 The initial part of the $\tau_L - s_L$ curves in the graph a is linear. In fact for small slips the interface is undamaged and the relationship between $\boldsymbol{\sigma}$ and $\mathbf{s}$ is linear, see Equations (4) and (11) with $\alpha^{(k)} = 0$.

The final branches of the $\tau_L - s_L$ curves in the graph are linear and horizontal. These branches correspond to the interface being fully damaged, with $\alpha^{(k)} = 1$ for every plane. In this condition, Equation (4) becomes $\boldsymbol{\sigma}^{(k)} = \boldsymbol{\sigma}_d^{(k)}$ and, since the interface considered is flat and the slip unidirectional and monotonic, the frictional law provides the only contribution to the tangential stress, equal to $\boldsymbol{\tau}_d = -\mu \left\langle \sigma_n \right\rangle_- \hat{\mathbf{v}}$ where $\hat{\mathbf{v}}$ is the slip direction, i.e. $\hat{\mathbf{v}} = (\partial \mathbf{s}/\partial t)/ \parallel \partial \mathbf{s}/\partial t \parallel$.

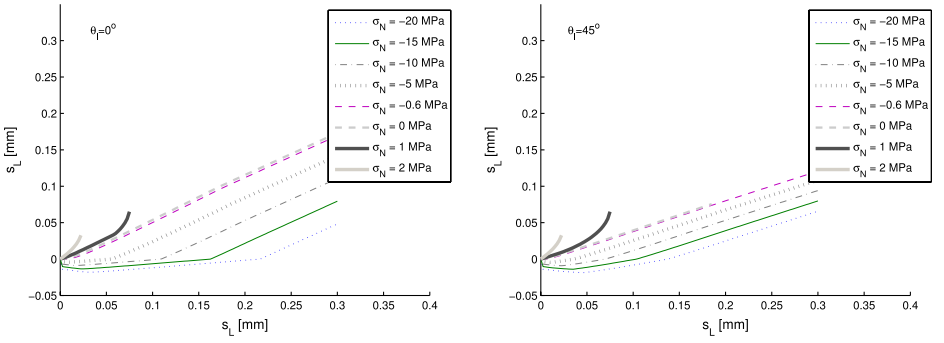

Figure 8. Dilation-slip ($s_n - s_L$) curves with $\theta_m = 30°$, monotonic load history along (a) $\theta_L = 0°$ and (b) $\theta_L = 45°$.

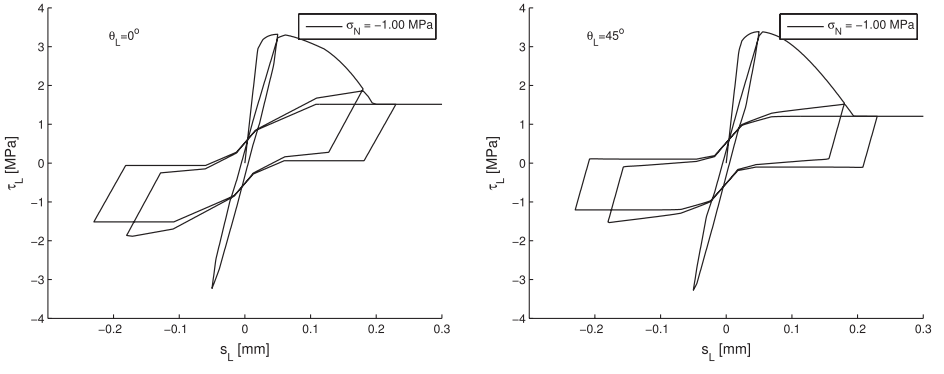

Figure 9. $\tau_L - s_L$ curves with $\theta_m = 30°$, cyclic load history along (a) $\theta_L = 0°$ and (b) $\theta_L = 45°$.

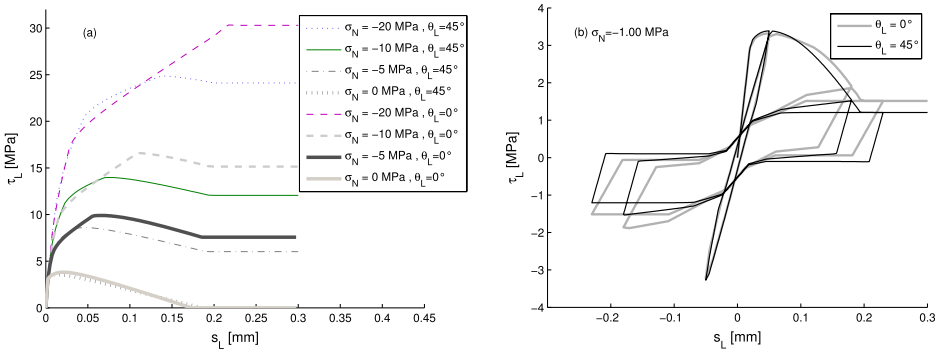

Figure 10. Comparison between the $\tau_L - s_L$ curves obtained for $\theta_L = 0°$ and $\theta_L = 45°$. (a): monotonic load history; (b): cyclic loading history ($\theta_m = 30°$).

The central concave part of the $\tau_t - s_t$ curves in the graph 4 a, between the initial and final linear branches, is originated while microplanes are undergoing progressive damage. □

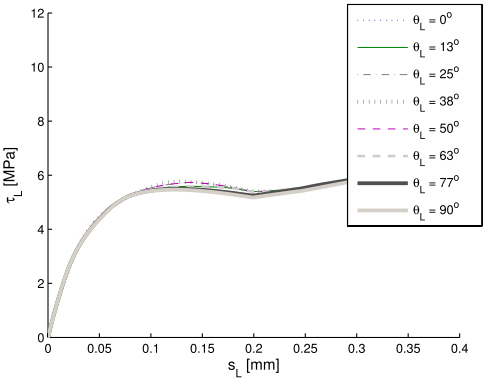

Figure 11. $\tau_L - s_L$ curves with $\boldsymbol{\sigma}_N = -5MPa, \theta_m = 30°$ and variable θ_L.

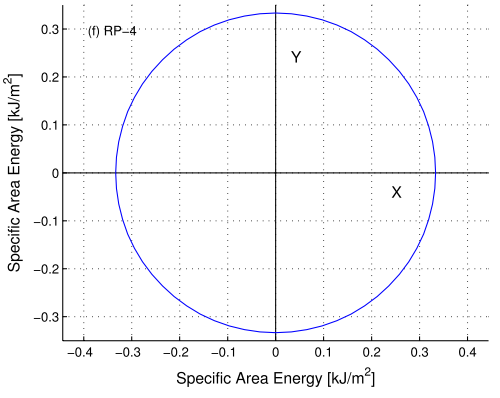

Figure 12. Polar plot of the total measured fracture energy versus θ_L with $\boldsymbol{\sigma}_N = 0$ and $\theta_m = 30°$.

4.2. 3D-Pattern with five microplanes

To investigate the interface response determined by a fully three-dimensional RIE, a second set of simulations were performed using the RIE composed of five microplanes with equal area fraction, ($\gamma^{(k)} = 0.2$, k=1,...,5) and components of the normal vectors specified in Table 3. The schematic view of the RIE is the one shown in Figure 1. The pattern is composed of one plane oriented as the average plane and four additional planes inclined by an angle θ_m to the average orientation. The numeration of the planes is shown in Figure 1. The material parameters employed in the simulations are again those of Table 2.

The simulations were performed applying a constant confining normal stress $\boldsymbol{\sigma}_n$ and a sliding $\mathbf{s}_L$ along a prefixed constant direction in the $T_x - T_y$ plane. Angle θ_L defines the direction of the impressed sliding with the T_x axis as depicted in Figure 6. Introducing the unit vector $\mathbf{e}_L = \frac{\mathbf{s}_L}{\|\mathbf{s}_L\|}$, the scalar and vector projection of the stress with $\mathbf{e}_L$ are denoted by τ_L and $\boldsymbol{\tau}_L$, respectively.

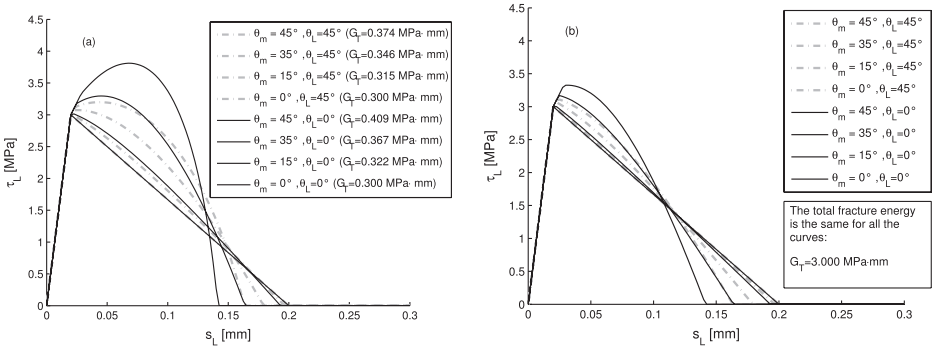

Figure 13. (a) $\tau_L - s_L$ curves with θ_m spanned in $[0°, 45°]$, monotonic load history along $\theta_L = 0°$ and $\theta_L = 45°$. The total measured fracture energy G_T is reported in the legend of (a). Plots in (b) are obtained considering the same numerical analyses of (a), setting instead zero friction ($\mu = 0$). Despite the curves being different in (b), the total measured fracture energy is the same for all curves.

Four types of analyses were carried with the RIE of Table 3. Specifically:

- Figure 7 shows the family of $\tau_L - s_L$ curves for $\boldsymbol{\sigma}_N$ spanned in the interval $[-20\,MPa, 2\,MPa]$, with microplanes inclined by $\theta_m = 30°$, a monotonic load history along the directions $\theta_L = 0°$ and $\theta_L = 45°$, obtained with $\eta = 0.99$;
- Figure 8 shows the corresponding dilatation curves;
- Figure 9 shows the family of $\tau_L - s_L$ curves for a fixed value of $\boldsymbol{\sigma}_N$, a fixed inclination $\theta_m = 30°$, $\eta = 0.9$, under a cyclic load history along the directions $\theta_L = 0°$ and $\theta_L = 45°$;
- Figure 10(a) and (b) shows a superposition of the curves in Figures 7 and 9.
- Figure 11 shows the family of $\tau_L - s_L$ curves for a fixed value of $\boldsymbol{\sigma}_N = -5\,MPa$, for a fixed inclination $\theta_m = 30°$ of the microplanes, with an impressed displacement s_L along angles θ_L spanned in the range $[0°, 90°]$;
- Figure 12 shows a polar graph of the total measured fracture energy versus θ_L, as derived by calculating the energy lost after a monotonic load history with increasing values of s_t and with $\theta_m = 30°$ and $\boldsymbol{\sigma}_N = 0$.

Figures 7 and 9 show that tau-slip curves depend on the direction of the displacement, i.e. the interface behaviour is anisotropic. Figures 10(a) and 10(b) point out the different behaviour for $\theta_L = 0°$ and $\theta_L = 45°$ and show that the anisotropy is more pronounced when a confinement pressure is applied.

It can be noted that the dilatation curves reported in Figure 8 present an unbounded character, i.e. the model is infinitely dilatant and the geometry of asperities does not evolve along the loading path. This is not a real limit of the model, as the present study is framed in the infinitesimal displament context, so that the values of the slip and, as a consequence, the dilatation are implicitly limited to be small compared to the asperities height. Indeed, a two-dimensional

multiplane model addressing a limited value for the dilatation has been proposed and assessed by numerical-experimental comparisons by Serpieri, Alfano et al. (2015).

4.3. Response for zero normal stress

In this subsection, the response obtained for $\boldsymbol{\sigma}_N = 0$, is examined closer in relation to the anisotropy of the energy response with respect to the sliding direction in the tangential plane. This case corresponds to an ideal pure mode II test if the mode is defined in terms of the interface stress components.

Figure 13(a) shows the family of $\tau_L - s_L$ curves for θ_m spanned in the interval $[0°, 45°]$ with $\sigma_N = 0$ and a monotonic loading history along the directions $\theta_L = 0°$ and $\theta_L = 45°$.

Figure 13(b) shows the results of the same simulations of Figure 13(a) considering instead a frictionless behaviour (μ=0) of the interface.

In both figures, the total fracture energy for each curve is reported in the relevant legends. This energy has been computed by numerically calculating the integral:

$$G_T = \int_0^{+\infty} \boldsymbol{\sigma}_L \, ds_L \tag{40}$$

applying the Simpson trapezoid integration method with displacement intervals of 0.0025mm.

Remark 4 It was shown in Figure 9(a) that, for $\boldsymbol{\sigma}_N = 0$, the tangential stress drops to zero when complete damage is reached. Instead, for $\boldsymbol{\sigma}_N < 0$, friction would occur also after complete damage and frictional dissipation after complete damage would contribute to the total energy. Hence, the second limit of integration in Equation (40) could not be $= \infty$ and would strongly influence the results. This is why the condition $\boldsymbol{\sigma}_N = 0$ is convenient to compare the model response for different θ_L. □

The following considerations can be drawn on the anisotropy of the energy response in relation to the sliding direction.

The linear elastic part of the graph is independent of both the angle of the microplanes and of the direction of the impressed displacement. This property shows that elastic anisotropy of the interface, which is captured instead by other interface formulations (see e.g. Rizzoni, Dumont, Lebon, & Sacco, 2014), is not captured by the present model. This feature is the direct consequence of constraint (12).

In the inelastic part of the curves, a significant increment of the tangential stress can be observed as the inclination of the microplanes is increased. This increment depends on the direction of sliding and shows the anisotropy of the interface. This

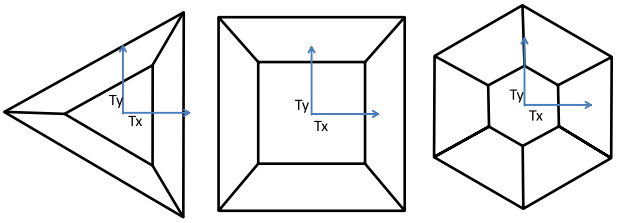

Figure 14. Schematic plan view of RP-3, RP-4, RP-6.

Table 4. 3D Surfaces used.

	RT	RP-3	RP-4	RP-6	RP-32
N_p	3	4	5	7	33
Inclined microplanes	2	3	4	6	32
$\gamma^{(k)}$ (for $k > 1$)	0.33333	0.22222	0.16667	0.11111	0.02083
Rotation angle $\zeta[^\circ]$	180	120	90	60	11.25

Table 5. Maximum and minumum total fracture energies and their ratio.

	RT	RP-3	RP-4	RP-6	RP-32
$G_{T,\max}[kJ]$	0.3475	0.3391	0.3338	0.3352	0.3332
$G_{T,\min}[kJ]$	0.2963	0.3241	0.3333	0.3312	0.3330
$G_{T,\max}/G_{T,min}$	1.1727	1.0463	1.0014	1.0120	1.0006

important effect is observed even when $\boldsymbol{\sigma}_N = 0$ and has been previously reported (Serpieri, Sacco, and Alfano, 2015) (see Figure 4 therein). The multiplane model predicts an increase of the total measured energy under increasing mode II/mode I ratio. This effect emerges from the interplay between adhesion, friction and interlocking, and vanishes whenever there is zero adhesion (prefractured interface), zero friction or zero interlocking (perfectly planar interface).

It is important to remark that the work spent to physically break the molecular bonds of the interface, which corresponds to the rupture energy discussed in Remark 1, is independent of the decohesion path and of the particular microplane arrangement employed. As a result, in Figure 13(b), where the effect of friction is excluded, despite the curves are different, the computed total fracture energy is independent of both the angle of the microplanes and of the direction of the impressed displacement. Conversely, the total measured fracture energy, which corresponds to the area under the tau-slip plots of Figure 13(a) obtained for $\boldsymbol{\sigma}_N = 0$ inclusive of the energy dissipated by friction, depends on both the decohesion path and angle of inclination of the microsurfaces (see related legends).

4.4. Sensitivity of anisotropy to RIE selection

The simulations of this last group were performed to investigate the sensitivity of the anisotropic behaviour of the model to the specific selection of the geometry

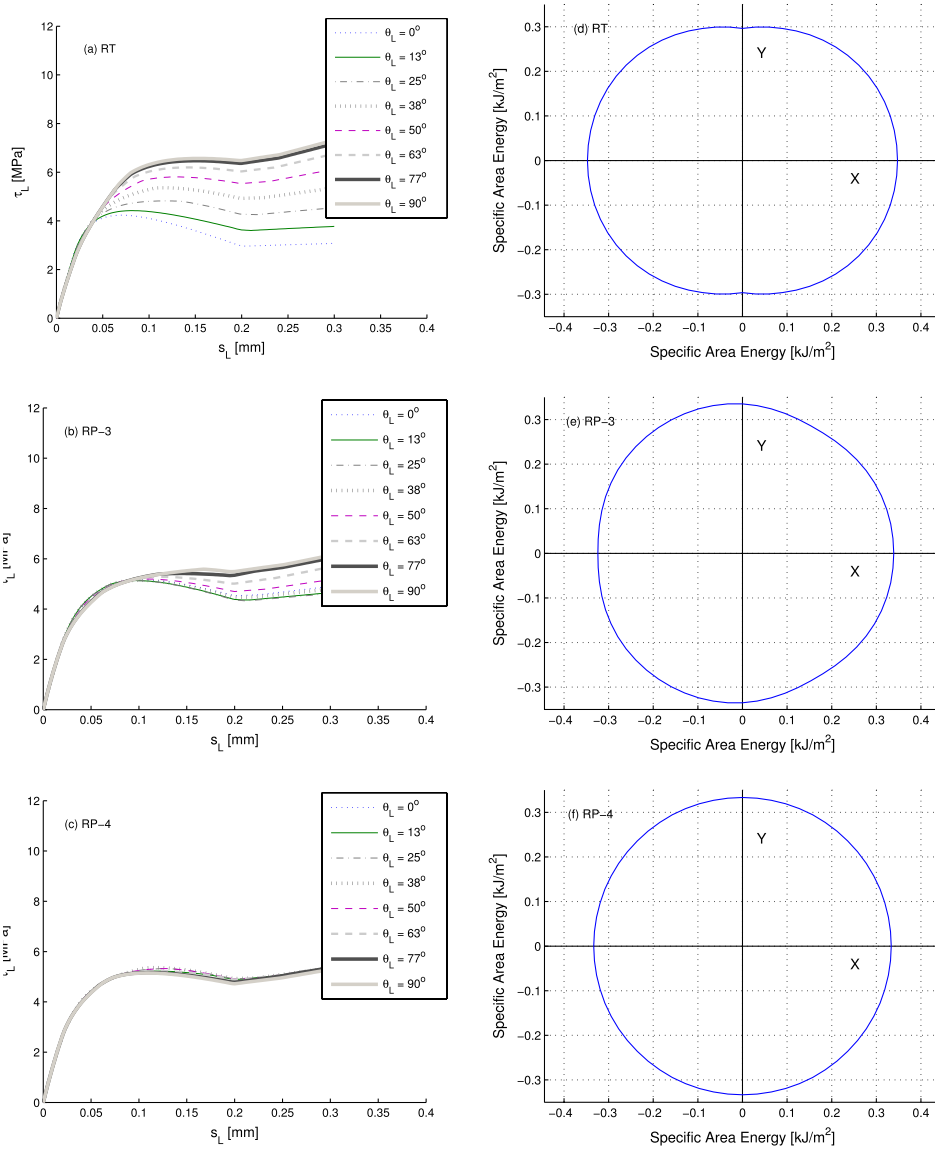

Figure 15. (a),(b),(c): diagrams of $\tau_L - s_L$ for a fixed value of $\boldsymbol{\sigma}_N = -5MPa$, with $\theta_m = 30°$ and monotonic load history along θ_L. (d),(e),(f): polar graphs of the total measured fracture energy as a function of θ_L with $\boldsymbol{\sigma}_N = 0$ and $\theta_m = 30°$ on the right.

and the number of inclined planes for the RIE. The RIE geometries examined in this section consist of four truncated pyramid shaped RIEs whose base is a regular polygon, plus an additional trapezoidal pattern with 2D symmetry of the type shown in Figure 3. Table 4 summarises the properties of the RIE patterns used. Each RIE has been denoted with a codename that is shown on the top of the table, with the following criteria:

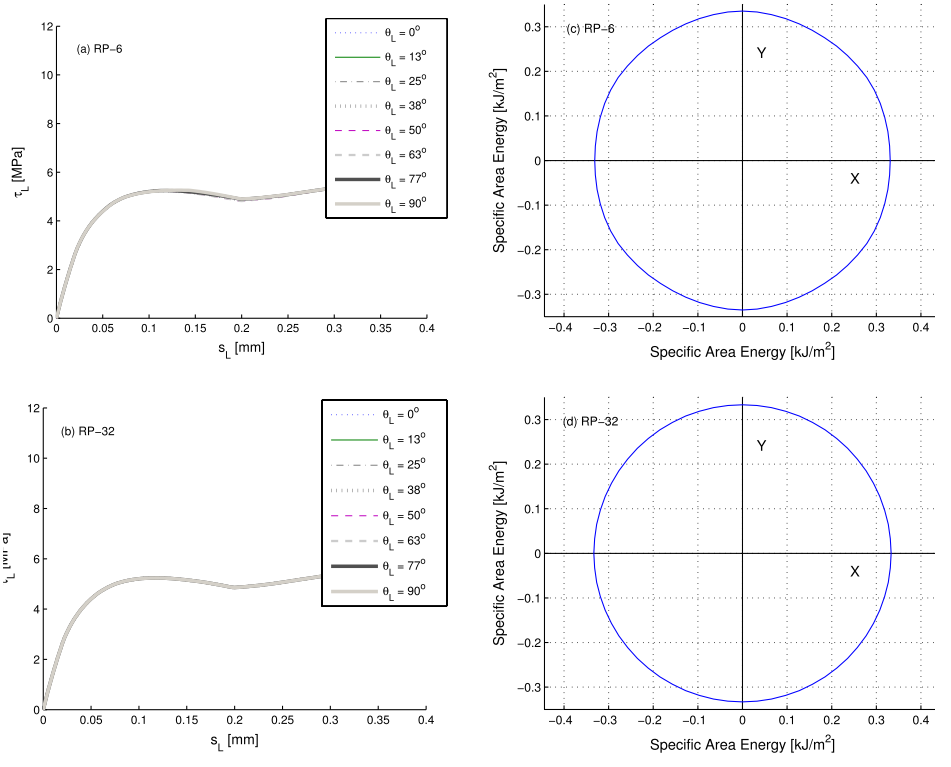

Figure 16. (a),(b): diagrams of $\tau_L - s_L$ for a fixed value of $\boldsymbol{\sigma}_N = -5MPa$, with $\theta_m = 30°$ and monotonic load history along θ_L. (c),(d): polar graph of the total measured fracture energy as a function of θ_L with $\boldsymbol{\sigma}_N = 0$ and $\theta_m = 30°$.

- RP-X (with $X = 3$, $X = 4$ or $X = 6$, $X = 32$) denotes a truncated pyramid shaped RIE whose base is a regular polygon with X sides, see Figure 14 and Figure 1;
- RT is the RIE shown in Figure 3.

Area fractions $\gamma^{(k)}$ are assigned with the following criterion: $1/3$ of the area to the horizontal microplane and $2/3$ are equally subdivided among the inclined microplanes. For RP-X patterns, the components of the normals to these surfaces are constructed as follows. The normal to the first inclined surface is set to

$$n^{(1)} = \begin{bmatrix} \cos\theta_m & -\sin\theta_m & 0 \end{bmatrix} \tag{41}$$

and the remaining normals are derived by rotating the first normal by the angle of rotation $\zeta = 2\pi/(N_p - 1)$ about the vertical axis (with unit vector[1 0 0]), (see Table 4), employing the formula:

$$\mathbf{n}^{(k)} = \mathbf{Q}^{(k)}\mathbf{n}^{(1)} \tag{42}$$

where

$$\mathbf{Q}^{(k)} = \begin{bmatrix} 1.0 & 0.0 & 0.0 \\ 0.0 & \cos((k-1)\zeta) & -\sin((k-1)\zeta) \\ 0.0 & \sin((k-1)\zeta) & \cos((k-1)\zeta) \end{bmatrix} \tag{43}$$

For each RIE the following plots are shown:

- $\tau_L - s_L$ for a fixed value of $\boldsymbol{\sigma}_N = -5\ MPa$, for a fixed inclination $\theta_m = 30°$ of the microplanes and with a prescribed displacement along θ_L which spans the range $[0°, 90°]$. The relevant plots are reported in Figures 15(a)–(c) and 16(a)–(c) on the left columns.
- a polar graph of the total measured fracture energy as a function of θ_L with $\boldsymbol{\sigma}_N = 0$ and $\theta_m = 30°$, obtained by post-computing the work spent after a single-sided load history with growing values of s_t according to Equation (40) and using again the Simpson rule with 0.0025mm increments. The relevant plots are reported in Figures 15 and 16 on the right columns.

Additionally, Table 5 shows the maximum and the minimum energies in the polar graphs of Figures 15 and 16 and their ratio. The maximum and the minimum reported energies were computed by evaluating the energy along 64 equally spaced directions and taking the maximum and the minimum value. The most interesting result in terms of practical implementation of the proposed model is that for the very simple and highly anisotropic geometry RP-3 the maximum difference in energy is lower than 5%, and for the relatively simple geometry RP-4 the difference is less than 0.2%, that is negligible for the vast majority of applications.

The graphs on Figures 15 and 16 confirm that the tau-slip curve and the total measured fracture energy depend on the direction of the displacement. The graphs on the left show that the tau-slip curves for different slip directions are coincident for low relative displacements, and increasingly different when relative displacements become higher. Since for low displacements the tau-slip curve is dominated by the linear behaviour of the undamaged interface and for high displacements by friction and damage (see remark 3), the anisotropic behaviour is mainly associated with the nonlinear effects of damage and friction. The plots also show that by increasing the number of sides of the RIE, the tau-slip curves for different directions of the displacements tend to overlap, and the polar plot of the apparent fracture energy approaches a perfect circle. This trend is highlighted in Table 5, which shows that the maximum and minimum energy ratio approaches unity as the number of sides increases.

5. Discussion and conclusions

In this paper, a 3D Cohesive zone model has been presented. The model has been developed as an extention of the 2D formulation presented by Serpieri and

Alfano (2011). A comparison with the 2D model has shown that the 3D model retrieves the 2D model behaviour, provided that a planar symmetric equivalent RIE is chosen. The behaviour of the model with a five microplanes RIE has been first investigated by comparing the behaviour of the interface when displacements along different direction are imposed. The relevant tau-slip plots have shown that the behaviour of the interface is anisotropic and that anisotropy is more pronounced when a confinement pressure is applied. A comparative study has been carried out using truncated pyramid RIEs with a regular polygon base to investigate the sensitivity of anisotropy to the choice of the RIE. This comparison has shown that, by employing more complex surfaces it is possible to approach an isotropic behaviour with the drawback of a higher computational cost. By increasing the number of sides of the polygon from 3 to 32, the difference between the maximum and the minimum total measured fracture energy drops from 4.7% to 0.6%, although the number of operations required grows more than eight times higher due to the higher number of microplanes (eight times) and due to the higher number of iterations required to attain convergence. On the other hand, if the RIE RP-3 is employed the maximum difference between maximum and minimum total fracture energy is less than 5%, which can be considered small for some applications. If RP-4 is employed, this difference is smaller than 0.2%, which is negligible for the vast majority of applications. Given the relatively small increase in computational cost between RP-3 and RP-4, the latter seems the optimal trade-off between computational complexity and accuracy for most applications of the multiplane interface model.

A further interesting potential application of the present multiplane approach is the simulation of the behaviour of interfaces that physically exhibit a nonisotropic sliding behaviour, (Konyukhov et al., 2008; Zmitrowicz, 2006) by employing RIE patterns that suitably reproduce asperities with anisotropic geometry.

Disclosure statement

No potential conflict of interest was reported by the authors.

Funding

This work was supported by the European Community [POR Campania FSE 2007-2013, CUP F82I11001150002].

References

Alfano, G., & Sacco, E. (2006). Combining interface damage and friction in a cohesive-zone model. *International Journal for Numerical Methods in Engineering, 68*, 542–582.

Allegri, G., Jones, M., Wisnom, M., & Hallett, S. (2011). A new semi-empirical model for stress ratio effect on mode II fatigue delamination growth. *Composites Part A: Applied Science and Manufacturing, 42*, 733–740.

Barton, N., & Choubey, V. (1977). The shear strength of rock joints in theory and practice. *Rock Mechanics, 10*(1–2), 1–54.

Bolzon, G., & Cocchetti, G. (2003). Direct assessment of structural resistance against pressurized fracture. *International Journal for Numerical and Analytical Methods in Geomechanics, 27*, 353–378.

Brown, S.R., & Scholz, C.H. (1985). Broad bandwidth study of the topography of natural rock surfaces. *Journal of Geophysical Research: Solid Earth (1978–2012)*, *90*, 12575–12582.

Červenka, J., Kishen, J. M. C., & Saouma, V. E. (1998). Mixed mode fracture of cementitious bimaterial interfaces; part II: Numerical simulation. *Engineering Fracture Mechanics, 60*, 95–107.

Charalambous, G., Allegri, G., Lander, J., & Hallett, S. (2015). A cut-ply specimen for the mixed-mode fracture toughness and fatigue characterisation of FRPs. *Composites Part A: Applied Science and Manufacturing, 74*, 77–87.

Cocchetti, G., Maier, G., & Shen, X. P. (2001). Piecewise linear models for interfaces and mixed mode cohesive cracks. *Computer Modeling in Engineering and Sciences, 3*, 279–298.

Cuvilliez, S., Feyel, F., Lorentz, E., & Michel-Ponnelle, S. (2012). A finite element approach coupling a continuous gradient damage model and a cohesive zone model within the framework of quasi-brittle failure. *Computer Methods in Applied Mechanics and Engineering, 237*, 244–259.

Del Piero, G., & Raous, M. (2010). A unified model for adhesive interfaces with damage, viscosity, and friction. *European Journal of Mechanics -- A/Solids, 29*, 496–507.

Evangelista, F., Roesler, J. R., & Proença, S. P. (2013). Three-dimensional cohesive zone model for fracture of cementitious materials based on the thermodynamics of irreversible processes. *Engineering Fracture Mechanics, 97*, 261–280.

Fouchal, F., Lebon, F., Raffa, M. L., & Vairo, G. (2014). An interface model including cracks and roughness applied to masonry. *Open Civil Engineering Journal, 8*, 263–271.

Fouchal, F., Lebon, F., & Titeux, I. (2009). Contribution to the modelling of interfaces in masonry construction. *Construction and Building Materials, 23*, 2428–2441.

Foulk, J. W., Allen, D. H., & Helms, K. L. E. (2000). Formulation of a three-dimensional cohesive zone model for application to a finite element algorithm. *Computer Methods in Applied Mechanics and Engineering, 183*, 51–66.

Gasser, T. C., & Holzapfel, G. A. (2006). 3D crack propagation in unreinforced concrete: A two-step algorithm for tracking 3D crack paths. *Computer Methods in Applied Mechanics and Engineering, 195*, 5198–5219.

Giambanco, G., Rizzo, S., & Spallino, R. (2001). Numerical analysis of masonry structures via interface models. *Computer Methods in Applied Mechanics and Engineering, 190*, 6493–6511.

Ho, S. L., Joshi, S. P., &Tay, A. (2012). *Cohesive zone modeling of 3D delamination in encapsulated silicon devices*. In *2012 IEEE 62nd Electronic Components and Technology Conference (ECTC)* (pp. 1493–1498), San Diego, CA.

Konyukhov, A., Vielsack, P., & Schweizerhof, K. (2008). On coupled models of anisotropic contact surfaces and their experimental validation. *Wear, 264*, 579–588.

Kuhn, H. W., & Tucker, A. W. (1951). Nonlinear programming. In *Proceedings of 2nd Berkeley symposium on mathematical statistics and probability* (pp. 481–492). Berkeley, CA: University of California Press.

Lee, H. S., Park, Y. J., Cho, T. F., & You, K. (2001). Influence of asperity degradation on the mechanical behavior of rough rock joints under cyclic shear loading. *International Journal of Rock Mechanics and Mining Sciences, 38*, 967–980.

Licht, C., & Michaille, G. (1997). A modelling of elastic adhesive bonded joints. *Advances in Mathematical Sciences and Applications, 7*, 711–740.

Licht, C., Michaille, G., & Pagano, S. (2007). A model of elastic adhesive bonded joints through oscillation-concentration measures. *Journal de mathématiques pures et appliquées, 87*, 343–365.

Luciano, R., & Sacco, E. (1997). Homogenization technique and damage model for old masonry material. *International Journal of Solids and Structures, 34*, 3191–3208.

Macorini, L., & Izzuddin, B. A. (2011). A non-linear interface element for 3D mesoscale analysis of brick-masonry structures. *International Journal for Numerical Methods in Engineering, 85*, 1584–1608.

Mauge, C., & Kachanov, M. (1994). Effective elastic properties of an anisotropic material with arbitrarily oriented interacting cracks. *Journal of the Mechanics and Physics of Solids, 42*, 561–584.

Mi, Y., Crisfield, M. A., Davies, G. A. O., & Hellweg, H. B. (1998). Progressive delamination using interface elements. *Journal of Composite Materials, 32*, 1246–1272.

Musto, M., & Alfano, G. (2015). *A fractional rate-dependent cohesive-zone model. International Journal for Numerical Methods in Engineering, 105*, 313–341.

Radovitzky, R., Seagraves, A., Tupek, M., & Noels, L. (2011). A scalable 3D fracture and fragmentation algorithm based on a hybrid, discontinuous Galerkin, cohesive element method. *Computer Methods in Applied Mechanics and Engineering, 200*, 326–344.

Rafsanjani, S. H., Loureno, P. B., & Peixinho, N. (2014). Dynamic interface model for masonry walls subjected to high strain rate out-of-plane loads. *International Journal of Impact Engineering, 76*, 28–37.

Raous, M., Cangémi, L., & Cocu, M. (1999). A consistent model coupling adhesion, friction, and unilateral contact. *Computer Methods in Applied Mechanics and Engineering, 177*, 383–399.

Rizzoni, R., Dumont, S., Lebon, F., & Sacco, E. (2014). Higher order model for soft and hard elastic interfaces. *International Journal of Solids and Structures, 51*, 4137–4148.

Ruiz, G., Pandolfi, A., & Ortiz, M. (2001). Three-dimensional cohesive modeling of dynamic mixed-mode fracture. *International Journal for Numerical Methods in Engineering, 52*, 97–120.

Serpieri, R., & Alfano, G. (2011). Bond-slip analysis via a thermodynamically consistent interface model combining interlocking, damage and friction. *International Journal for Numerical Methods in Engineering, 85*, 164–186.

Serpieri, R., Alfano, G., & Sacco, E. (2015). A mixed-mode cohesive-zone model accounting for finite dilation and asperity degradation. *International Journal of Solids and Structures, 67–68*, 102–115.

Serpieri, R., Sacco, E., & Alfano, G. (2015). A thermodynamically consistent derivation of a frictional-damage cohesive-zone model with different mode I and mode II fracture energies. *European Journal of Mechanics - A/Solids, 49*, 13–25.

Serpieri, R., Varricchio, L., Sacco, E., & Alfano, G. (2014). Bond-slip analysis via a cohesive-zone model simulating damage, friction and interlocking. *Fracture and Structural Integrity, 29*, 284–292.

Simo, J. C., & Hughes, T. J. R. (2008). *Computational inelasticity*. New York, NY : Springer.

Snozzi, L., & Molinari, J. F. (2013). A cohesive element model for mixed mode loading with frictional contact capability. *International Journal for Numerical Methods in Engineering, 93*, 510–526.

Sørensen, B. F., & Jacobsen, T. K. (2009). Characterizing delamination of fibre composites by mixed mode cohesive laws. *Composites Science and Technology, 69*, 445–456.

Van den Bosch, M. J., Schreurs, P. J. G., & Geers, M. G. D. (2008). On the development of a 3D cohesive zone element in the presence of large deformations. *Computational Mechanics, 42*, 171–180.

Zmitrowicz, A. (2006). Models of kinematics dependent anisotropic and heterogeneous friction. *International Journal of Solids and Structures, 43*, 4407–4451.